Interevent Variability in Ground-Motion Prediction Models: The Role of the Source Parameter Selection

Dino Bindi*[1], Adrien Oth[2], Stefano Parolai[3], Matteo Picozzi[4], and Daniele Spallarossa[5]

ABSTRACT

We investigate the dependence of interevent residuals on the choice of source parameters used in ground-motion prediction models calibrated for peak ground acceleration, peak ground velocity, and peak ground displacement. Using a dataset of 877,566 recordings from 1586 earthquakes with magnitudes ranging from 1 to 6.5 in central-southern Italy, we perform multiple mixed-effects regressions, exploring different approaches for the source scaling component. We compare the interevent standard deviation of models based on various source parameters, including moment magnitude, local magnitude, radiated energy, source spectral value at 3 Hz, moment magnitude with stress drop, and moment magnitude with apparent stress. Our results show that combining moment magnitude with either stress drop or apparent stress yields the lowest variability across all peak parameters, as expected. In addition, using local magnitude effectively captures the stress-drop-related component of variability. For the analyzed magnitude range, the source spectral amplitude at 3 Hz performs similarly to local magnitude in this regard, without saturating for large magnitudes. These findings suggest that source parameter choices complementary or alternative to moment magnitude can help reduce interevent variability. However, the suitability of models based on parameters other than moment magnitude depends on the specific application.

OPEN ACCESS

KEY POINTS

- Most of the ground-motion models use self-similar scaling, controlled solely by seismic moment.
- We assess how different source parameters and magnitude scales affect interevent variability.
- Local and spectral magnitudes (e.g., at 3 Hz) better capture high-frequency ground-motion variability.

INTRODUCTION

Probabilistic seismic hazard assessment (PSHA) estimates the expected annual rate of exceedance for different thresholds of a given ground-motion parameter of engineering interest. This is achieved through the hazard integral, which marginalizes the probability distribution of ground motion over all possible earthquake magnitudes and source-to-site distances (McGuire and Arabasz, 1990). Within the PSHA framework, the ground-motion prediction model (GMPM) computes the normal probability distribution of the expected ground motion for any considered earthquake scenario. A GMPM consists of two key components: (1) a model describing how the median ground motion scales with magnitude and distance for a given site condition, and (2) a standard deviation quantifying the apparent aleatory variability around the median prediction.

The moment magnitude **M**, as defined by Hanks and Kanamori (1979), is the primary explanatory variable used in most modern GMPMs to describe source scaling of the median model. From the Aki (1966) perspective, GMPMs typically assume self-similar scaling, in which a single-source parameter, that is, the seismic moment, is sufficient to characterize the source spectrum. However, when a GMPM is developed from a dataset containing events with identical seismic moments but different high-frequency source radiation, systematic differences in the generated ground shaking are shifted to the interevent (or between-event) residuals (Atik *et al.*,

1. GFZ Helmholtz Centre for Geosciences, Potsdam, Germany, https://orcid.org/0000-0002-8619-2220 (DB); 2. European Center for Geodynamics and Seismology, Walferdange, Luxembourg, https://orcid.org/0000-0003-4859-6504 (AO); 3. Department of Mathematics, Informatics and Geosciences, University of Trieste, Trieste, Italy, https://orcid.org/0000-0002-9084-7488 (SP); 4. National Institute of Oceanography and Applied Geophysics, Center for Seismological Research, Udine, Italy, https://orcid.org/0000-0001-8078-9416 (MP); 5. Department of Earth Sciences of Environment and Life, University of Genova, Genova, Italy, https://orcid.org/0000-0002-8021-3908 (DS)

*Corresponding author: dino.bindi@gfz.de

Cite this article as Bindi, D., A. Oth, S. Parolai, M. Picozzi, and D. Spallarossa (2025). Interevent Variability in Ground-Motion Prediction Models: The Role of the Source Parameter Selection, *Bull. Seismol. Soc. Am.* **115**, 2857–2866, doi: 10.1785/0120250098

2010). The interevent residuals quantify repeated source effects affecting the recordings of a given event not modeled by the median model. A well-documented example in the literature concerns the dependence of the high-frequency radiation on stress drop. Because events with the same seismic moment but different stress drops produce different levels of high-frequency shaking, and because most GMPMs do not explicitly incorporate stress drop as an explanatory variable, the interevent residuals at moderate-to-high frequencies exhibit a positive correlation with stress drop (Bindi *et al.*, 2007, 2018; Baltay *et al.*, 2013; Oth *et al.*, 2017; Bindi and Kotha, 2020; Nie and Wang, 2025). In addition to stress drop, other source parameters, particularly rupture velocity, also influence high-frequency radiation. The interplay between stress drop and rupture velocity and their combined impact on key ground-motion parameters such as peak ground acceleration (PGA) has been explored in various studies of both laboratory and tectonic events (e.g., Causse and Song, 2015; Passelègue *et al.*, 2020). In this study, we adopt a simplified approach using the stress drop estimated from the corner frequency of an ω^2 source model as a proxy for high-frequency radiation. This assumes, on average, a constant rupture velocity across events. In this study, we investigate how interevent variability is affected by considering source parameters different from moment magnitude, such as the local magnitude or the radiated energy. We also examine the impact of incorporating additional source parameters along with the moment magnitude, namely the stress drop and the apparent stress (Picozzi *et al.*, 2018b). Finally, following the idea of introducing magnitude scales based on the high-frequency source spectral level (Atkinson and Hanks, 1995), we also investigate the impact on the interevent residuals of considering the source spectral amplitude at 3 Hz (Street *et al.*, 1975; Parolai *et al.*, 2024). Using a dataset from central Italy, we develop multiple GMPMs with different source parameter choices and compare the resulting interevent variability for PGA, peak ground velocity (PGV), and displacement.

DATA

We consider the data set analyzed by Bindi *et al.* (2024; Figs. 1, 2). It is composed by 877,566 recordings generated by 28,939 earthquakes recorded at 955 stations. The considered events have magnitude range from 1 to 6.5, recorded at hypocentral distances smaller than 120 km, and we selected stations and events with at least three recordings. The data set was processed by Bindi *et al.* (2024) to isolate the source spectra from propagation and site effects through a generalized inversion technique. The source spectra were in turn fit to an ω^2 model (Brune, 1970) to estimate the seismic moment M_0 and the corner frequency f_c. In this study, we consider the following source parameters:

- moment magnitude **M**, computed as $\mathbf{M} = (\log M_0 - 9.1)/1.5$ (Hanks and Kanamori, 1979);

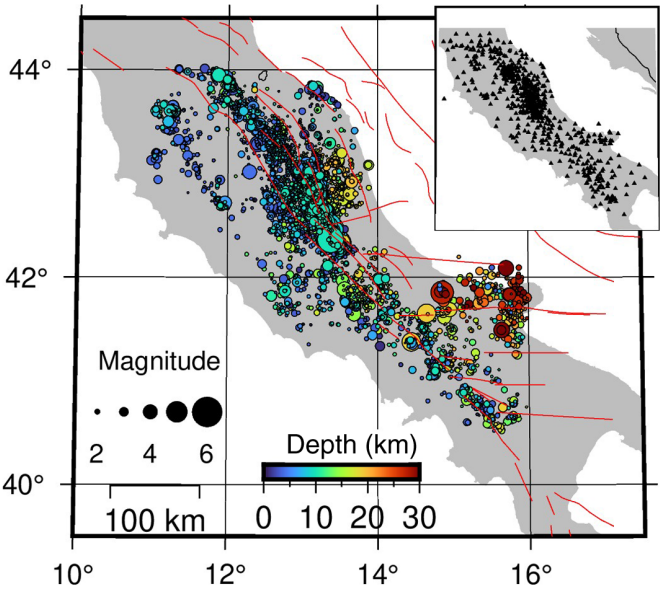

Figure 1. Earthquake locations in the analyzed dataset for central Italy. Circles represent earthquake events, with colors indicating hypocentral depth and radius proportional to magnitude. The inset map shows the locations of seismic stations. The red lines sketch the main active faults considered for probabilistic seismic hazard assessment (PSHA) in Europe (see Data and Resources). The color version of this figure is available only in the electronic edition.

- stress drop $\Delta\sigma$, computed considering a circular rupture of radius r with uniform stress drop (Eshelby, 1957; Keilis-Borok, 1959; Brune, 1970):

$$r = \frac{0.37\beta}{f_c}, \tag{1}$$

$$\Delta\sigma = \frac{7}{16}\frac{M_0}{r^3}, \tag{2}$$

in which the shear-wave velocity at the hypocentral locations β is taken from Menichelli *et al.* (2023);
- radiated energy E_r (Venkataraman and Kanamori, 2004), computed from the integral of the squared velocity source spectrum corrected for limited bandwidth effects (Ide and Beroza, 2001);
- apparent stress σ_a (Wyss, 1970), computed as $\sigma_a = \mu E_r/M_0$, assuming for the shear modulus the average value of $\mu = 30$ GPa;
- the amplitude at 3 Hz of the acceleration source spectra $S(f)$ as provided by the nonparametric spectral decomposition performed by Bindi *et al.* (2024), $S3 = \log S(f = 3\text{ Hz})$; and
- the local magnitude M_L (Richter, 1935), calibrated in this study for the considered data. The M_L values are constrained to be unbiased with respect to **M** by correcting for the average difference between M_L and M evaluated for **M** between 3 and 5.

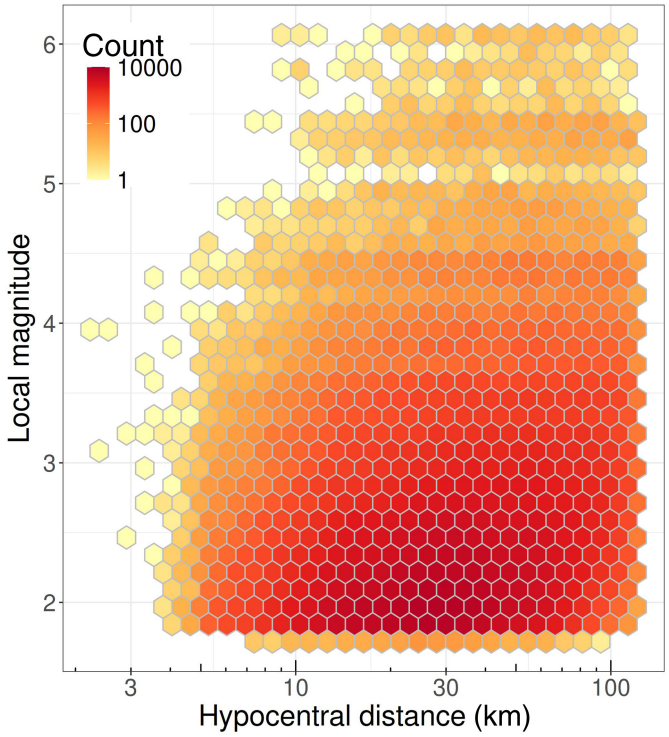

Figure 2. Magnitude versus distance density plot for the analysed data set, considering the Fourier spectral amplitudes available at 2 Hz. The color version of this figure is available only in the electronic edition.

Figure 3 shows the scaling of the considered source parameters. Both $\log(\Delta\sigma)$ and $\log(\sigma_a)$ have been centered to their mean values. The following observations can be drawn from Figure 3:

1. Figure 3a shows that, on average, M_L and **M** exhibit a nearly one-to-one scaling, with deviations around the median trend correlated with $\Delta\sigma$. The relationship between $\Delta\sigma$ and **M**–M_L differences have been observed in multiple studies (e.g., Bindi, Zaccarelli, and Kotha, 2020, their fig. 15) and discussed by Deichmann (2017);
2. Figure 3b shows that $S3$ and **M** follow a more quadratic trend, with residuals somewhat related to $\Delta\sigma$, aligning with theoretical expectations from the Brune model (see Fig. 4);
3. Figure 3c shows that the scaling of $\Delta\sigma$ with **M** exhibits a positive trend below a certain magnitude (between 4 and 5), after which it tends to remain constant. For magnitudes below 4, variability increases, and there are potentially finite-bandwidth censoring effects below magnitude 2. This study does not investigate the impact of possible heteroskedasticity affecting the source parameter distributions on ground motion;
4. Figure 3d shows that stress drop and apparent stress are in strong agreement, suggesting minimal differences in using one versus the other;
5. Figure 3e shows that $S3$ and M_L align well, with discrepancies mainly for small events, likely due to their corner frequencies exceeding 3 Hz (Fig. 4); see also Parolai *et al.* (2024, their figure 1); and
6. Figure 3f shows that $S3$ scales with radiated energy, though scatter increases for smaller events, primarily controlled by $\Delta\sigma$. As shown in Figure 4, when the magnitude is small enough, 3 Hz falls below the corner frequency, rendering S_3 nearly insensitive to $\Delta\sigma$ variations. Conversely, radiated energy, being dependent on the entire spectrum, increases with $\Delta\sigma$ for a given magnitude.

The difficulty of resolving the corner frequency of small events in central Italy has been thoroughly investigated by Bindi, Spallarossa, *et al.* (2020). The authors demonstrated that the variance of the source parameters increases below magnitudes of 2.5–3 and that the estimates can be biased below magnitude 2. To ensure reliable estimates of source parameters unaffected by bandwidth limitations, in the following we consider only the 15,871 events with $\mathbf{M} \geq 2$, that is, $\log M_0 \geq 12.1$.

MODEL

We use a mixed-effects regression (Bates *et al.*, 2015) to calibrate different GMPMs for PGA, PGV, and peak ground displacement (PGD), based on the following functional form:

$$\log(PGx) = c_0 + F_{D1} + F_{D2} + F_M + \delta B_e + \delta S2S + \epsilon, \quad (3)$$

in which PGx is indicating one of the three considered peak parameters. The scaling with distance terms F_{D1} and F_{D2} are described by the following equations:

$$F_{D1} = \begin{cases} n_1 \log(60/R) + n_2 \log(10/60) & \text{for } R \leq 60 \text{ km} \\ n_2 \log(10/R) & R > 60 \text{ km} \end{cases}, \quad (4)$$

$$F_{D2} = \begin{cases} 0 & \text{for } R \leq 20 \text{ km} \\ n_3(R - 20) & \text{for } R > 20 \text{ km} \end{cases}, \quad (5)$$

in which a piece-wise linear model is implemented for the geometrical spreading term with hinge distance at 60 km (equation 4), and an anelastic term is considered for distances above 20 km (equation 5). Because the data set is dominated by magnitudes below 4 with only five events with magnitude above 5.5 (Fig. 2), the distance scaling terms F_{D1} and F_{D2} are not accounting for the saturation at short distances.

Regarding the source scaling term F_M, we calibrate multiple GMPMs by considering alternative choices for the source parameters that control F_M:

$$F_M = b_1(\mathbf{M} - 3), \quad (6)$$

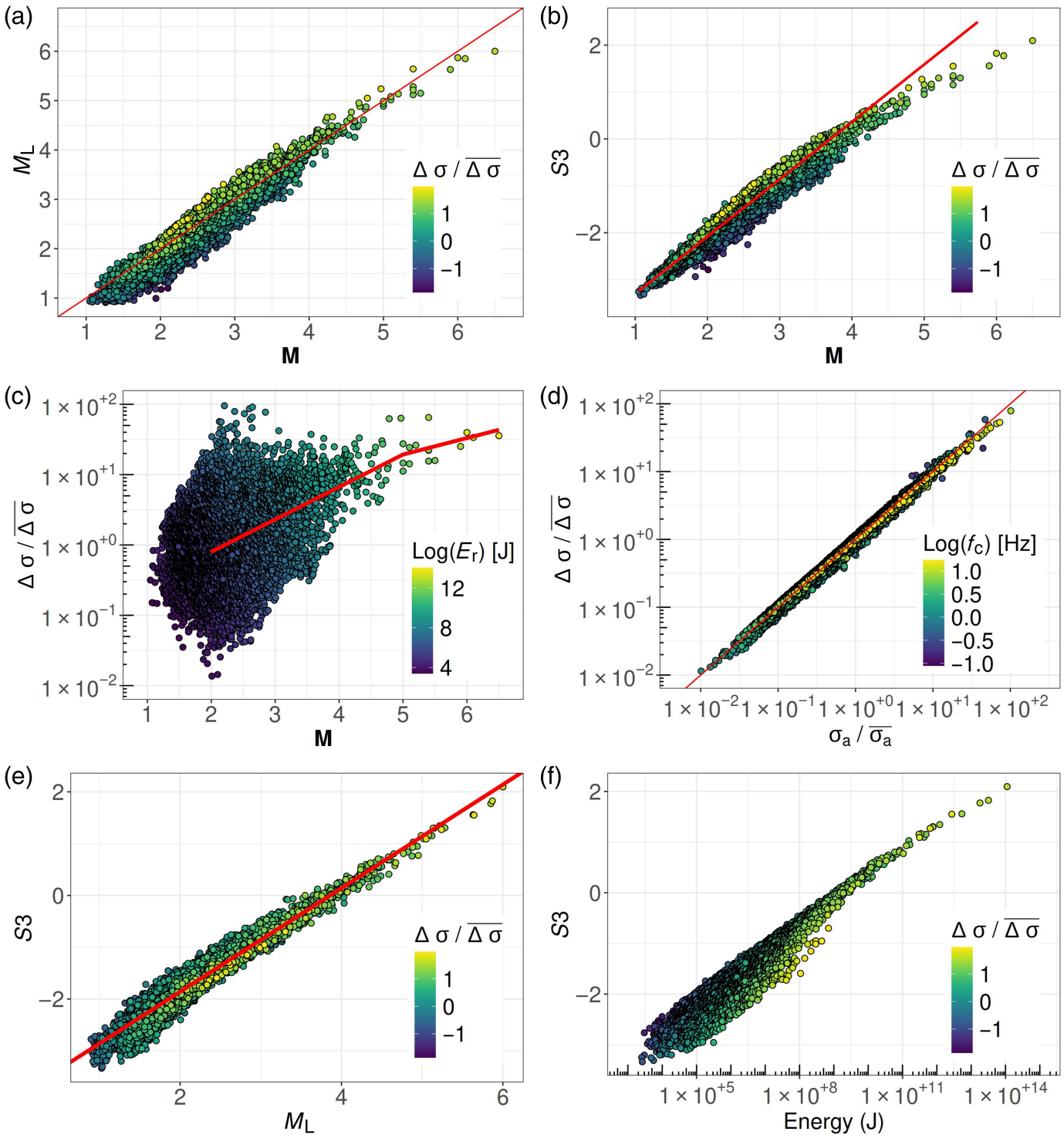

$$F_M = b_2(M_L - 3), \tag{7}$$

$$F_M = b_3(\mathbf{M} - 3) + b_4(\log(\Delta\sigma) - \overline{\log(\Delta\sigma)}), \tag{8}$$

$$F_M = b_5(\mathbf{M} - 3) + b_6(\log(\sigma_a) - \overline{\log(\sigma_a)}), \tag{9}$$

$$F_M = b_7(\log(E_r) - 6), \tag{10}$$

Figure 3. Scaling of different source parameters is considered for developing the ground-motion prediction models (GMPMs). The red lines in the different panels represent: (a) one-to-one relationship, (b) best-fitting linear model in a least-squares sense, (c) best piece-wise linear model obtained with a segmented regression (fixing the breakpoint at M 5), (d) one-to-one relationship, and (e) best-fitting linear model. The color version of this figure is available only in the electronic edition.

$$F_M = b_8(S_3 + 1.5), \quad (11)$$

in which the overlying bar in equations (8) and (9) indicates the mean value. In equation (3), the overall residuals are partitioned into the interevent (δBe) and interstation ($\delta S2S$) residuals, whereas the leftovers are indicated with ϵ. The δBe, $\delta S2S$, and ϵ random effects are zero-mean normal distributions with standard deviations τ, ϕ_{S2S}, and ϕ_0, respectively. The target of this study is to compare the standard deviations of the random effects and, in particular, τ for the different choices and combinations of the source parameters (equations 6–11).

RESULTS

The regression results, expressed in terms of the standard deviation of the random effects, are presented in Figure 5. Different symbols represent: the total standard deviation σ (black circles), between-station standard deviation ϕ_{S2S} (gray squares), between-event deviation τ (red triangles), and leftovers standard deviation ϕ_0 (white diamonds). Figure 5 confirms that ϕ_{S2S} contributes the most to the total variability (Atik *et al.*, 2010) across all three peak ground motion parameters. This contribution is the highest for PGA and similar for PGV and PGD. Regarding ϕ_0, which accounts for the not modeled path and source-to-station effects, it remains almost constant across all peak parameters and models. The behavior of τ (between-event variability) depends on the choice of source-scaling variables and the selected peak ground-motion parameter:

- for PGA, τ is the largest when only **M** is considered. The lowest values occur when incorporating both **M** and $\Delta\sigma$ or σ_a, as well as in the model using E_r. The models using M_L and $S3$ yield intermediate τbetween those of the models using only **M** and those including **M** and $\Delta\sigma$;
- for PGV, τ follows a trend similar to PGA, but for PGV, the models incorporating E_r, M_L and $S3$ yield nearly the same τ as those including **M** and $\Delta\sigma$ or σ_a; and
- for PGD: τ is lower when using **M** than when using E_r. The model based on $S3$ results have lower τ compared to M_L. As with the other peak parameters, the lowest τ values are obtained when **M** is combined with $\Delta\sigma$ or σ_a.

Because frequency content shifts toward lower frequencies moving from acceleration to velocity and displacement, the observed trends in Figure 5 align with expectations. The between-event residuals obtained for the models using **M**, M_L, and $S3$ are shown in Figure 6 versus stress drop. The correlation observed between interevent residuals and $\Delta\sigma$ when using **M** (Pearson correlation coefficient $\rho_P \sim 0.75$ for all PGx) decreases significantly when either M_L or S_3 source parameters are considered, particularly for PGV ($\rho_P = 0.24$ and 0.36 for M_L and S_3, respectively) and PGD ($\rho_P \sim 0$). In addition, Figure 6 shows that for PGA and PGV, hypocentral depth contributes to increased variability, with events deeper than 15–20 km showing a distinctive pattern (not further investigated in this study).

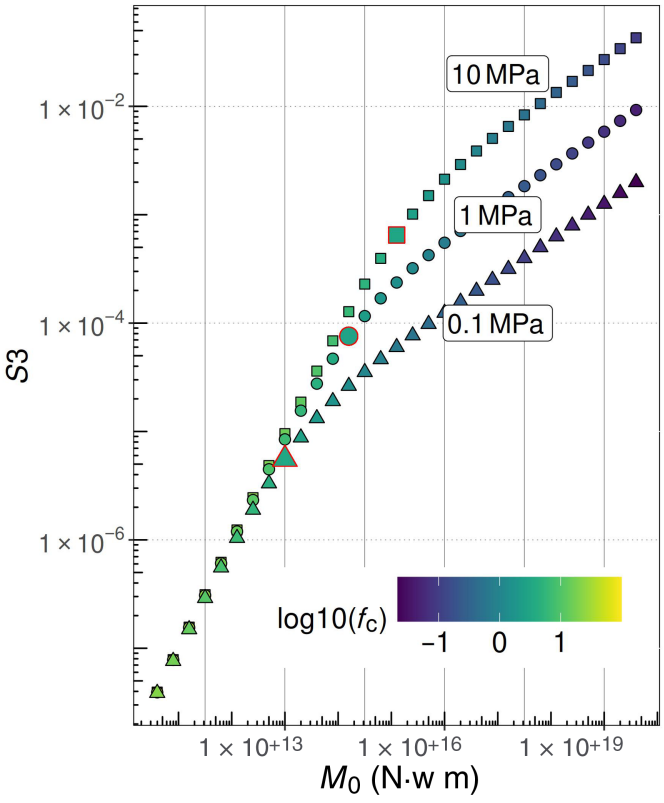

Figure 4. S3 scaling with seismic moment for Brune's model, considering three different $\Delta\sigma$ values. Corner frequencies equal to 3 Hz for the three scalings are indicated by the larger symbols. The color version of this figure is available only in the electronic edition.

DISCUSSION

Although the complexity of earthquake source processes cannot be fully captured by a single parameter (Bormann and Di Giacomo, 2011; Picozzi *et al.*, 2018a), most GMPMs assume source self-similarity, considering only seismic moment to control source scaling. Since the early development of GMPMs, residual analyses have indicated that seismic moment alone is insufficient and should be complemented, for example, by stress drop to accurately describe source scaling across a wide frequency range (Trifunac and Brady, 1976), in particular when small and moderate events are also considered. However, the predictive nature of GMPMs has historically prevented stress drop, or any other parameter that can be a proxy for high-frequency ground motion, from being included as an explanatory variable (Campbell, 1985). As a result, only a few GMPMs have incorporated stress drop as a predictive parameter (e.g., Bora *et al.*, 2015; Ameri *et al.*, 2017; Sgobba *et al.*, 2023). Figure 5 demonstrates that incorporating stress drop alongside seismic moment improves the ability to capture source effects across a broad frequency range, both at long

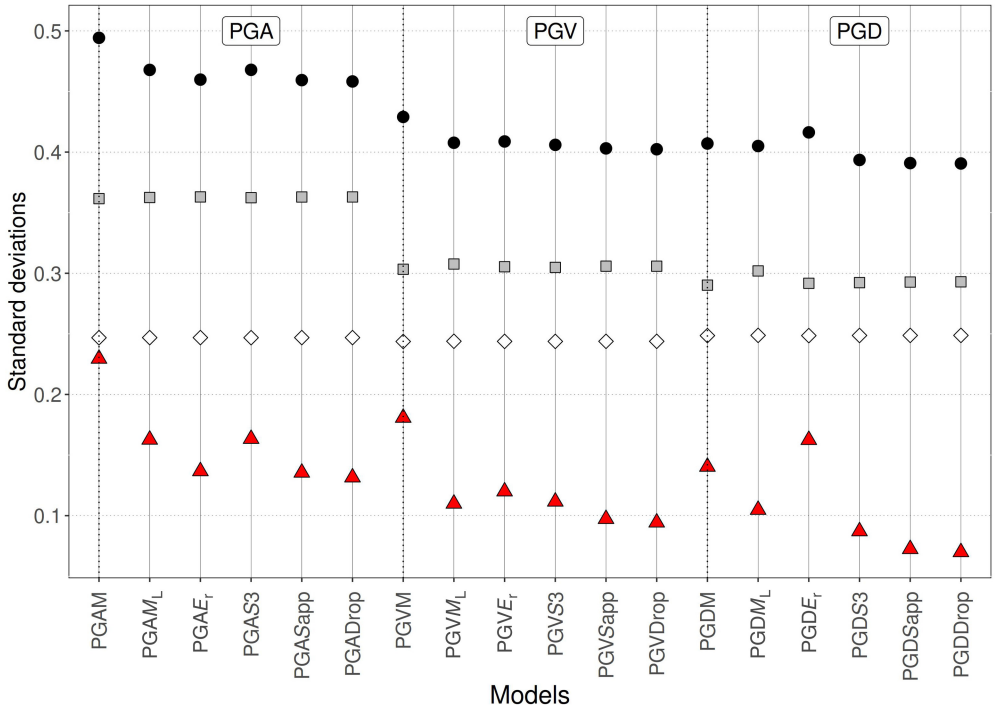

Figure 5. Standard deviations of the models calibrated for peak ground acceleration (PGA), peak ground velocity (PGV), and peak ground displacement (PGD) considering different source parameters. The interevent standard deviation τ is shown as red triangles, the total standard deviation σ as black circles, the station-specific ϕ_{S2S} in gray. and ϕ_0 as white diamonds. Considering PGA, the results for **M** (equation 4) are indicated with PGA**M**, for M_L (equation 5) with PGAM_L, for E_r (equation 8) with PGAE_r, for *S*3 (equation 9) with PGA*S*3, for **M** and σ_a (equation 7) with PGA*S*app, for **M** and $\Delta\sigma$ (equation 6) with PGADrop. Similar names are used for PGV and PGD. The color version of this figure is available only in the electronic edition.

periods, where scaling is controlled by seismic moment, and at frequencies above the corner frequency, where source spectra are sensitive to stress-drop variations. However, stress-drop estimates are subject to significant uncertainty (Abercrombie, 2021), which can introduce substantial epistemic uncertainty in GMPMs, potentially offsetting any reduction in aleatory variability when assessing, for example, seismic hazard both for urban planning and seismic design. Moreover, the large uncertainties and model dependencies associated with stress-drop estimates continue to drive debate over its scaling with seismic moment and its variability with depth (Abercrombie *et al.*, 2021). These challenges, along with ongoing discussions about whether stress-drop values for small events can be used to constrain those of larger earthquakes (Hardebeck, 2020), hinder the ability to define region-specific reference stress-drop values essential for predictive applications.

One possible approach is to develop multilayered GMPMs that allow switching between a basic, stress-drop-independent model and a more advanced, stress-drop-dependent layer. This would be useful for regions where data are available to allow stress-drop computation with an acceptable level of uncertainty (Sgobba *et al.*, 2023). Alternatively, incorporating different magnitude scales or source parameters could enhance flexibility in capturing source-related ground-motion variability. Several studies have explored the effect of using alternative magnitude scales or source parameters to better represent the variability of ground shaking at high frequencies.

One such example is m_N (Nuttli, 1973), developed for stable continental settings. m_N is based on the maximum amplitude of *Lg* waves, which dominate the 1–5 Hz frequency range. Street *et al.* (1975) compared the seismic moment of 78 earthquakes in the Central United States with both surface-wave magnitude (M_s) and body-wave magnitude (m_b). Notably, the authors interpreted distance-corrected *Lg* spectra in terms of Brune's source model and demonstrated that the empirical relationship between seismic moment and corner frequency captures the transition between earthquakes with average stress drops of 0.1–0.6 MPa. Assuming that a magnitude defined for a given signal period is proportional to the logarithm of the source spectrum at the same period, they introduced $m_{0.3}$ and $m_{0.1}$, corresponding to m_N evaluated considering the source spectral amplitude at 0.3 (~3 Hz) and 0.1 s (10 Hz), respectively. By anchoring these two scales to m_b, they extended the applicability of m_b to micro-earthquakes, accounting for source radiation effects at frequencies exceeding 1 Hz as considered by m_b.

The concept of considering the high-frequency spectral level was further advanced by Atkinson and Hanks (1995), who introduced the high-frequency magnitude as a complement to **M** to better constrain the impact of source parameters such as $\Delta\sigma$ on ground shaking. More recently, Parolai *et al.* (2024) revisited this idea by proposing a new magnitude scale based on an estimate of the source spectral amplitude at 3 Hz, aiming to better capture high-frequency radiation effects. The choice of 3 Hz is particularly relevant because it corresponds to a frequency range of interest for residential buildings. In addition, sensitivity analyses within the framework of PSHA have shown that stress-drop sensitivity is the highest around 3 Hz (Molkenthin *et al.*, 2014; Dif *et al.*, 2020). Figure 5 demonstrates that, for the considered dataset, the use of *S*3 reduces the standard deviation τ of interevent variability compared

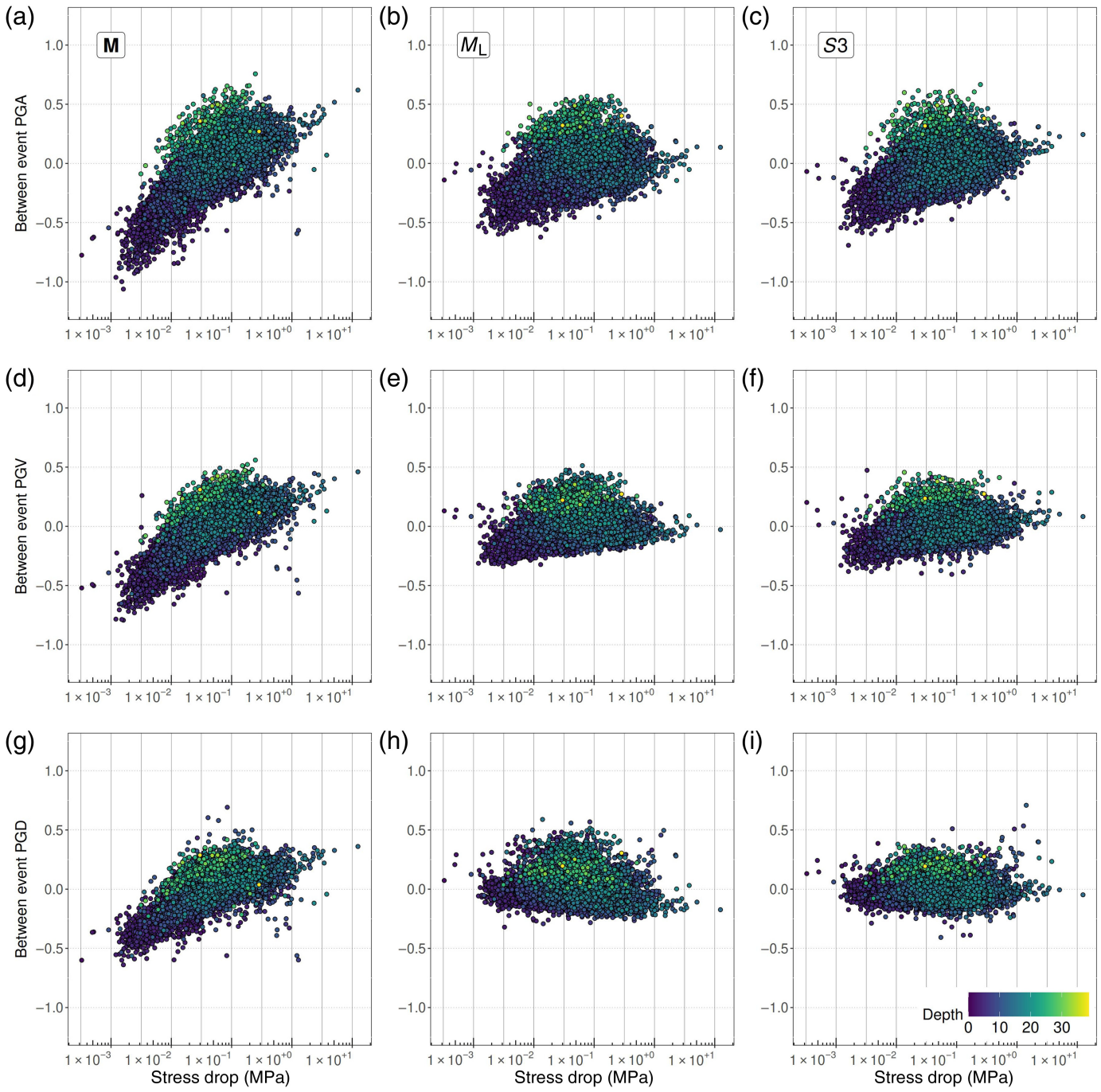

Figure 6. Interevent residuals versus stress drop, with colors indicating hypocentral depth. Results for (a–c) PGA, (d–f) PGV, and (g–i) PGD are shown from top to bottom; results for **M**, Ml, and S3 are shown from left to right. The color version of this figure is available only in the electronic edition.

to **M** for PGA, PGV, and high-pass filtered PGD. Notably, the performance of *S*3 is comparable to that of the widely used local magnitude M_L. Because M_L depends on both seismic moment M_0 and stress drop $\Delta\sigma$ (Deichmann, 2017), it effectively captures the influence of $\Delta\sigma$ variability in small-to-moderate events. Previous studies comparing interevent residuals and their standard deviation τ for models calibrated on **M** and M_L across different regions (e.g., Central Italy, Türkiye, and Ridgecrest) have shown that M_L helps reduce τ at intermediate frequencies, particularly for PGV. However, a known limitation of M_L is its saturation for magnitudes above ~6. This does not affect S_3, which is based on the spectral amplitude of the source acceleration spectrum (Parolai *et al.*, 2024). Efforts have been made to develop non-saturating magnitude scales that align with M_L in which it remains valid but extends to larger events without saturation (e.g., Kanamori *et al.*, 1993). Nevertheless, the challenge of capturing stress-drop variability is more critical for small and moderate events

(Fig. 3c), whereas for larger ones, moment magnitude **M** may suffice. It is also worth noting that magnitude scales can have limitations at the lower end. For example, for events small enough to shift the corner frequency above 3 Hz ($M_0 \sim 10^{13}$ N · m, **M** ∼ 2.6), the Brune source spectral amplitude at 3 Hz becomes insensitive to $\Delta\sigma$ variations (Fig. 4). Depending on the specific application, limitations at either the low- or high-magnitude end may influence the choice of the most appropriate source parameter for analysis.

Finally, Figure 5 suggests that using $\log E_r$ (or energy magnitude), which accounts for energy across a broad frequency range, is optimal for PGA and PGV. However, for PGD, its effectiveness may be limited due to high-pass filtering effects. Moreover, the computation of radiated energy requires corrections for high-frequency attenuation effects, particularly for small events, which can introduce significant epistemic uncertainties in GMPMs using E_r as explanatory variable.

CONCLUSIONS

Site-specific ground-motion analysis can benefit from a reduction in interevent variability (τ), especially in applications for which the site-to-site variability is excluded from the aleatory uncertainty, such as single-station (onsite) earthquake early warning (Spallarossa *et al.*, 2018), or nonergodic PSHAs (Anderson and Brune, 1999). In addition, model frameworks that reduce τ can support investigations into potential preparatory phases preceding large earthquakes (e.g., Picozzi *et al.*, 2019; Picozzi *et al.*, 2024), enhancing our ability to detect subtle changes in source characteristics prior to rupture. Compared to models based solely on moment magnitude, we quantified the reduction of τ achieved by incorporating additional source parameters, such as the stress drop or the apparent stress, into GMPMs for PGA, PGV, and PGD.

However, the use of stress drop as a predictive parameter is limited by substantial uncertainties in its estimation and its low predictability. To address these challenges, we tested the performance of alternative magnitude scales and source parameters, including the local magnitude (M_L), the radiated energy (E_r), and the source spectral amplitude at 3 Hz ($S3$). Within the moment magnitude range from 2 to 6.5 analyzed in this study, $S3$ and M_L demonstrated comparable effectiveness in reducing τ for PGA, PGV, and PGD, as they capture variations in source spectral levels near and above the corner frequency among earthquakes with the same seismic moment. Potential limitations of M_L may arise for larger events in which magnitude saturation effects could occur. However, for large earthquakes, the assumption of self-similarity appears to hold, suggesting that **M** alone may be sufficient to describe source scaling in GMPMs. Regarding $S3$, theoretical expectations based on the Brune model indicate that for earthquakes below **M** ∼ 2.6, its sensitivity to stress-drop variability diminishes. More importantly for hazard-oriented studies, however, a magnitude based on $S3$ does not saturate for large events (Parolai *et al.*, 2024).

In conclusion, alternative or complementary source parameters to **M** can help reduce the interevent variability at high frequencies. The optimal approach depends on data availability, parameter reliability, and the specific objectives of the GMPM application. In the context of probabilistic hazard assessment, incorporating new variables into GMPMs requires additional levels of integration or joint probability density functions that account for parameter correlation when marginalizing the hazard integral. Furthermore, adopting alternative magnitude scales necessitates access to well-developed catalogs and the ability to evaluate magnitude recurrence distributions (Parolai *et al.*, 2024). The development of Bayesian approaches for GMPMs could enhance model flexibility, allowing for the integration of varying levels of information across different regions and facilitating model updates as new data become available.

DATA AND RESOURCES

We use data from the following networks: IV (Istituto Nazionale di Geofisica e Vulcanologia [INGV], 2005), IT (Presidency of Counsil of Ministers - Civil Protection Department, 1972), MN (MedNet Project Partner Institutions, 2018), OT (University of Bari "Aldo Moro", 2013), GU (University of Genoa, 1967), GE (GEOFON Data Centre, 1993), VD (CNR IMAA Consiglio Nazionale delle Ricerche [Italy], 2019), XO (EMERSITO Working Group, 2018), YR (Segou *et al.*, 2016), XJ (Voisin *et al.*, 2009), 4A (Istituto Nazionale di Geofisica e Vulcanologia [INGV], 2009), 3A (Istituto Nazionale di Geofisica e Vulcanologia [INGV], Istituto di Geologia Ambientale e Geoingegneria [CNR-IGAG], Istituto per la Dinamica dei Processi Ambientali [CNR-IDPA], Istituto di Metodologie per l'Analisi Ambientale [CNR-IMAA], and Agenzia Nazionale per le nuove tecnologie, l'energia e lo sviluppo economico sostenibile [ENEA], 2018), TV (INGV experiments network, not registered), IX (Irpinia Seismic Network ISNet, not registered). Analyses have been performed in R (R Core Team, 2024); Figure 1 has been prepared with Generic Mapping Tool (GMT; Wessel *et al.*, 2019); fault traces in Figure 1 are taken from http://www.efehr.org (last accessed July 2025).

DECLARATION OF COMPETING INTERESTS

The authors acknowledge that there are no conflicts of interest recorded.

ACKNOWLEDGMENTS

The authors would like to thank Gabriele Ameri and Associate Editor Sanjay Bora for their constructive comments and valuable suggestions, which have helped improve the clarity and quality of their article.

REFERENCES

Abercrombie, R. E. (2021). Resolution and uncertainties in estimates of earthquake stress drop and energy release, *Phil. Trans. Roy. Soc. Lond. A* **379,** no. 2196, 20200131.

Abercrombie, R. E., D. T. Trugman, P. M. Shearer, X. Chen, J. Zhang, C. N. Pennington, J. L. Hardebeck, T. H. W. Goebel, and C. J. Ruhl (2021). Does earthquake stress drop increase with depth in the crust? *J. Geophys. Res.* **126,** no. 10, e2021JB022314, doi: 10.1029/2021JB022314.

Aki, K. (1966). Generation and propagation of g waves from the Niigata earthquake of June 16, 1964. Part 2. Estimation of earthquake moment, released energy, and stress-strain drop from the g wave spectrum, *Bull. Earthq. Res. Inst. Univ. Tokyo* **44,** no. 1, 73–88.

Ameri, G., S. Drouet, P. Traversa, D. Bindi, and F. Cotton (2017). Toward an empirical ground motion prediction equation for France: accounting for regional differences in the source stress parameter, *Bull. Earthq. Eng.* **15,** 4681–4717.

Anderson, J. G., and J. N. Brune (1999). Probabilistic seismic hazard analysis without the ergodic assumption, *Seismol. Res. Lett.* **70,** no. 1, 19–28.

Atik, L. A., N. Abrahamson, J. J. Bommer, F. Scherbaum, F. Cotton, and N. Kuehn (2010). The variability of ground-motion prediction models and its components, *Seismol. Res. Lett.* **81,** no. 5, 794–801.

Atkinson, G. M., and T. C. Hanks (1995). A high-frequency magnitude scale, *Bull. Seismol. Soc. Am.* **85,** no. 3, 825–833.

Baltay, A. S., T. C. Hanks, and G. C. Beroza (2013). Stable stress-drop measurements and their variability: Implications for ground-motion prediction, *Bull. Seismol. Soc. Am.* **103,** no. 1, 211–222.

Bates, D., M. Mächler, B. Bolker, and S. Walker (2015). Fitting linear mixed-effects models using lme4, *J. Stat. Softw.* **67,** no. 1, 1–48.

Bindi, D., and S. R. Kotha (2020). Spectral decomposition of the engineering strong motion (ESM) flat file: Regional attenuation, source scaling and Arias stress drop, *Bull. Earthq. Eng.* **18,** 2581–2606.

Bindi, D., S. Parolai, H. Grosser, C. Milkereit, and E. Durukal (2007). Empirical ground-motion prediction equations for northwestern Turkey using the aftershocks of the 1999 Kocaeli earthquake, *Geophys. Res. Lett.* **34,** no. 8, doi: 10.1029/2007GL029222.

Bindi, D., D. Spallarossa, M. Picozzi, and P. Morasca (2020). Reliability of source parameters for small events in Central Italy: Insights from spectral decomposition analysis applied to both synthetic and real data, *Bull. Seismol. Soc. Am.* **110,** no. 6, 3139–3157.

Bindi, D., D. Spallarossa, M. Picozzi, D. Scafidi, and F. Cotton (2018). Impact of magnitude selection on aleatory variability associated with ground-motion prediction equations: Part I–local, energy, and moment magnitude calibration and stress-drop variability in central Italy, *Bull. Seismol. Soc. Am.* **108,** no. 3, 1427–1442.

Bindi, D., D. Spallarossa, M. Picozzi, and G. Tarchini (2024). Scaling and depth variability of source parameters in central and southern italy using regional attenuation models, *Bull. Seismol. Soc. Am.* doi: 10.1785/0120240144.

Bindi, D., R. Zaccarelli, and S. R. Kotha (2020). Local and moment magnitude analysis in the Ridgecrest region, California: Impact on interevent ground-motion variability, *Bull. Seismol. Soc. Am.* **111,** no. 1, 339–355.

Bora, S. S., F. Scherbaum, N. Kuehn, P. Stafford, and B. Edwards (2015). Development of a response spectral ground-motion prediction equation (GMPE) for seismic-hazard analysis from empirical Fourier spectral and duration models, *Bull. Seismol. Soc. Am.* **105,** no. 4, 2192–2218.

Bormann, P., and D. Di Giacomo (2011). The moment magnitude Mw and the energy magnitude Me: common roots and differences, *J. Seismol.* **15,** no. 2, 411–427.

Brune, J. N. (1970). Tectonic stress and the spectra of seismic shear waves from earthquakes, *J. Geophys. Res.* **75,** no. 26, 4997–5009.

Campbell, K. W. (1985). Strong motion attenuation relations: A ten-year perspective, *Earthq. Spectra* **1,** no. 4, 759–804.

Causse, M., and S. G. Song (2015). Are stress drop and rupture velocity of earthquakes independent? Insight from observed ground motion variability, *Geophys. Res. Lett.* **42,** no. 18, 7383–7389.

CNR IMAA Consiglio Nazionale delle Ricerche (Italy) (2019). High Agri valley geophysical observatory, *International Federation of Digital Seismograph Networks*, doi: 10.7914/SN/VD.

Deichmann, N. (2017). Theoretical basis for the observed break in ml/mw scaling between small and large earthquakes, *Bull. Seismol. Soc. Am.* **107,** no. 2, 505–520.

Dif, Z., B. Derras, F. Cotton, and C. Molkenthin (2020). Data-driven testing of the magnitude dependence of earthquake stress parameters using the nga-west2 dataset, *J. Seismol.* **24,** no. 6, 1095–1107.

EMERSITO Working Group (2018). Rete Sismica del Gruppo Emersito, Sequenza Sismica del 2016 in Italia Centrale, *International Federation of Digital Seismograph Networks*, doi: 10.13127/sd/7txegdo5x8.

Eshelby, J. D. (1957). The determination of the elastic field of an ellipsoidal inclusion, and related problems, *Proc. Math. Phys. Sci.* **241,** no. 1226, 376–396.

GEOFON Data Centre (1993). GEOFON seismic network, *International Federation of Digital Seismograph Networks*, doi: 10.14470/TR560404.

Hanks, T. C., and H. Kanamori (1979). A moment magnitude scale, *J. Geophys. Res.* **84,** no. B5, 2348–2350.

Hardebeck, J. L. (2020). Are the stress drops of small earthquakes good predictors of the stress drops of moderate-to-large earthquakes? *J. Geophys. Res.* **125,** no. 3, e2019JB018831, doi: 10.1029/2019JB018831.

Ide, S., and G. C. Beroza (2001). Does apparent stress vary with earthquake size? *Geophys. Res. Lett.* **28,** no. 17, 3349–3352.

Istituto Nazionale di Geofisica e Vulcanologia (INGV) (2005). Rete Sismica Nazionale (RSN), doi: 10.13127/SD/X0FXNH7QFY.

Istituto Nazionale di Geofisica e Vulcanologia (INGV) (2009). Emersito seismic network for site effect studies in L'Aquila town (Central Italy), *International Federation of Digital Seismograph Networks*, doi: 10.7914/SN/4A_2009.

Istituto Nazionale di Geofisica e Vulcanologia (INGV), Istituto di Geologia Ambientale e Geoingegneria (CNR-IGAG), Istituto per la Dinamica dei Processi Ambientali (CNR-IDPA), Istituto di Metodologie per l'Analisi Ambientale (CNR-IMAA), and Agenzia Nazionale per le nuove tecnologie, l'energia e lo sviluppo economico sostenibile (ENEA) (2018). Rete del Centro di Microzonazione Sismica (CentroMZ), sequenza sismica del 2016 in Italia Centrale [Data set], *Istituto Nazionale di Geofisica e Vulcanologia (INGV), International Federation of Digital Seismograph Networks*, doi: 10.13127/sd/ku7xm12yy9.

Kanamori, H., J. Mori, E. Hauksson, T. H. Heaton, L. K. Hutton, and L. M. Jones (1993). Determination of earthquake energy release and ml using terrascope, *Bull. Seismol. Soc. Am.* **83,** no. 2, 330–346.

Keilis-Borok, V. (1959). On estimation of the displacement in an earthquake source and of source dimensions, *Ann. Geophys* **12,** no. 2, 205–214.

McGuire, R. K., and W. J. Arabasz (1990). An introduction to probabilistic seismic hazard analysis, *Geotech. Environ. Geophys.* **1,** 333–354.

MedNet Project Partner Institutions (2018). Mediterranean very broadband seismographic network (MedNet), *Istituto Nazionale di Geofisica e Vulcanologia (INGV), International Federation of Digital Seismograph Networks*, doi: 10.13127/sd/fbbbtdtd6q.

Menichelli, I., P. De Gori, F. P. Lucente, L. Improta, and C. Chiarabba (2023). Lithosphere structure, processes, and physical state of the Alpine-Apennine system, *J. Geophys. Res.* **128,** no. 4, e2023JB026411, doi: 10.1029/2023JB026411.

Molkenthin, C., F. Scherbaum, A. Griewank, N. Kuehn, and P. Stafford (2014). A study of the sensitivity of response spectral amplitudes on seismological parameters using algorithmic differentiation, *Bull. Seismol. Soc. Am.* **104,** no. 5, 2240–2252.

Nie, S., and Y. Wang (2025). Revealing spatial variations of earthquake stress drop and peak ground acceleration using a non-ergodic modeling framework, *Geophys. Res. Lett.* **52,** no. 5, e2024GL112043, doi: 10.1029/2024GL112043.

Nuttli, O. W. (1973). Seismic wave attenuation and magnitude relations for eastern North America, *J. Geophys. Res.* **78,** no. 5, 876–885.

Oth, A., H. Miyake, and D. Bindi (2017). On the relation of earthquake stress drop and ground motion variability, *J. Geophys. Res.* **122,** no. 7, 5474–5492.

Parolai, S., D. Spallarossa, A. Oth, and M. Picozzi (2024). A proposal for a high-frequency earthquake magnitude (m3Hz) for seismic hazard and rapid damage assessment, *Seismol. Res. Lett.* doi: 10.1785/0220240226.

Passelègue, F. X., M. Almakari, P. Dublanchet, F. Barras, J. Fortin, and M. Violay (2020). Initial effective stress controls the nature of earthquakes, *Nat. Commun.* **11,** 5132.

Picozzi, M., D. Bindi, D. Spallarossa, A. Oth, D. Di Giacomo, and A. Zollo (2018a). Moment and energy magnitudes: diversity of views on earthquake shaking potential and earthquake statistics, *Geophys. J. Int.* **216,** no. 2, 1245–1259.

Picozzi, M., D. Bindi, D. Spallarossa, A. Oth, D. Di Giacomo, and A. Zollo (2018b). A rapid response magnitude scale for timely assessment of the high frequency seismic radiation, *Sci. Rep.* **8,** 8562.

Picozzi, M., D. Bindi, A. Zollo, G. Festa, and D. Spallarossa (2019). Detecting long-lasting transients of earthquake activity on a fault system by monitoring apparent stress, ground motion and clustering, *Sci. Rep.* **9,** 16,268.

Picozzi, M., D. Spallarossa, A. G. Iaccarino, and D. Bindi (2024). Event-specific ground motion anomalies highlight the preparatory phase of earthquakes during the 2016–2017 Italian seismicity, *Commun. Earth Environ.* **5,** 289.

Presidency of Counsil of Ministers - Civil Protection Department (1972). Italian strong motion network, *International Federation of Digital Seismograph Networks*, doi: 10.7914/SN/IT.

R Core Team (2024). *R: A Language and Environment for Statistical Computing*, R Foundation for Statistical Computing, Vienna, Austria.

Richter, C. F. (1935). An instrumental earthquake magnitude scale, *Bull. Seismol. Soc. Am.* **25,** no. 1, 1–32.

Segou, M., J. McCloskey, B. Baptie, and D. Hawthorn (2016). Armatrice sequence international, *International Federation of Digital Seismograph Networks*, doi: 10.7914/SN/YR_2016.

Sgobba, S., G. Lanzano, L. Colavitti, P. Morasca, M. C. D'Amico, and D. Spallarossa (2023). Physics-based parametrization of a FAS nonergodic ground motion model for Central Italy, *Bull Earthq. Eng.* **21,** 4111–4137.

Spallarossa, D., S. R. Kotha, M. Picozzi, S. Barani, and D. Bindi (2018). On-site earthquake early warning: a partially non-ergodic perspective from the site effects point of view, *Geophys. J. Int.* **216,** no. 2, 919–934.

Street, R. L., R. B. Herrmann, and O. W. Nuttli (1975). Spectral characteristics of the lg wave generated by central united states earthquakes, *Geophys. J. Int.* **41,** no. 1, 51–63.

Trifunac, M. D., and A. G. Brady (1976). Correlations of peak acceleration, velocity and displacement with earthquake magnitude, distance and site conditions, *Earthq. Eng. Struct. Dynam.* **4,** no. 5, 455–471.

University of Bari "Aldo Moro" (2013). OTRIONS, *International Federation of Digital Seismograph Networks*, doi: 10.7914/SN/OT.

University of Genoa (1967). Regional Seismic Network of North Western Italy, *International Federation of Digital Seismograph Networks*, doi: 10.7914/SN/GU.

Venkataraman, A., and H. Kanamori (2004). Effect of directivity on estimates of radiated seismic energy, *J. Geophys. Res.* **109,** no. B4, doi: 10.1029/2003JB002548.

Voisin, C., A. Mariscal, A. Hok-Schlagenhauf, G. Salaun, P. Traversa, and RESIF (2009). Seismic network XJ: French part of L AQUILA (Italy) aftershock experiment (RESIF-SISMOB), doi: 10.15778/RESIF.XJ2009.

Wessel, P., J. F. Luis, L. Uieda, R. Scharroo, F. Wobbe, W. H. F. Smith, and D. Tian (2019). The generic mapping tools version 6, *Geochem. Geophys. Geosys.* **20,** no. 11, 5556–5564.

Wyss, M. (1970). Stress estimates for south American shallow and deep earthquakes, *J. Geophys. Res.* **75,** no. 8, 1529–1544.

Manuscript received 1 May 2025
Published online 27 August 2025